

Collective charge excitations between moiré-minibands in twisted WSe₂ bilayers from resonant inelastic light scattering

Nihit Saigal,¹ Lennart Klebl,² Hendrik Lambers,¹ Sina Bahmanyar,¹ Veljko Antić,¹ Dante M. Kennes,^{3,4} Tim O. Wehling,^{2,5} and Ursula Wurstbauer^{1,6}

¹*Institute of Physics, University of Münster, Wilhelm-Klemm-Str. 10, 48149 Münster, Germany*

²*Institute of Theoretical Physics, University of Hamburg, Notkestrasse 9, 22607 Hamburg, Germany*

³*Institute for Theory of Statistical Physics, RWTH Aachen University, and JARA Fundamentals of Future Information Technology, 52062 Aachen, Germany*

⁴*Max Planck Institute for the Structure and Dynamics of Matter, Center for Free Electron Laser Science, 22761 Hamburg, Germany*

⁵*The Hamburg Centre for Ultrafast Imaging, 22761 Hamburg, Germany*

⁶*Center for Soft Nanoscience (SoN), Busso-Peus-Str. 10, 48149 Münster, Germany**

(Dated: October 24, 2023)

We establish low-temperature resonant inelastic light scattering (RILS) spectroscopy as a tool to probe the formation of a series of moiré-bands in twisted WSe₂ bilayers by accessing collective inter-moiré-band excitations (IMBE). We observe resonances in such RILS spectra at energies in agreement with inter-moiré band (IMB) transitions obtained from an *ab-initio* based continuum model. Transitions between the first and second IMB for a twist angle of about 8° are reported and between first and second, third and higher bands for a twist of about 3°. The signatures from IMBE for the latter highlight a strong departure from parabolic bands with flat minibands exhibiting very high density of states in accord with theory. These observations allow to quantify the transition energies at the K-point where the states relevant for correlation physics are hosted.

Twisted van der Waals (vdW) bilayers present a unique condensed matter platform to realize and control electronic correlation effects [1, 2]. The large scale superlattice created by the superposition of the two layers at a slight rotational mismatch defines a reciprocal mini-Brillouin zone with nearly dispersionless (flat) bands as long as the layers hybridize sufficiently. The drastically reduced kinetic energy, potentially together with van Hove physics, results in a very high density of states (DOS) in those flat bands favorable for driving electrons into the correlated regime. In several graphene-based systems correlated and ordered electronic phases are experimentally well-established [6–10]. In transition metal dichalcogenide (TMDC) based vdW stacks the absence of complications like topological obstructions have facilitated high-level microscopic many-body studies from early on [11] and explained the emergence of ordered, insulating and also different flavors of correlated metallic states of matter [12, 13]. Experimentally, the aforementioned correlation effects have been realized [14, 15], while superconductivity has remained elusive with currently one report of an (unclear and controversial) zero resistance state [14] even though there are multiple theoretical studies [16–18]. These emergent phases in semiconductor-based moiré bilayers are attributed to strongly interacting electronic K/K'-states.

In this letter, we experimentally access moiré minibands at the valence band maximum (VBM) around the K/K' valley by studying their collective electronic in-

ter moiré band excitations (IMBE) by resonant inelastic light scattering (RILS) experiment as summarized in Fig. 1. Accessing the moiré bands at the K-points is challenging for the combined reason of twist angle variations and reconstruction in realistic devices together with the VBM at the Γ and K-points being close in energy [19]. The morphology of twisted bilayers, particularly at small twist angles, is such that variations in twist angle, but also reconstruction (in plane as well as corrugation) plays an important role. This leads to periodically patterned areas different to those expected from a rigid moiré lattice-picture [20–23]. While these patterns result in rich optical interband spectra [23] and even host coherent many-body states of excitons [24], it makes the interpretation of spectroscopic signatures and the direct spectroscopy of moiré bands e.g. by angle-resolved photoemission spectroscopy (ARPES) difficult with only a few reports on selected materials combinations [25, 26]. Recent μ -ARPES and STM studies demonstrate the formation of moiré-bands at the valence band maximum (VBM) at the Γ -point of twisted WSe₂ bilayers [22, 27, 28]. Accessing moiré bands around the K, K' states and their properties is still lacking.

We remedy this standing problem by reporting on collective electronic excitations between moiré bands formed in twisted and hBN encapsulated WSe₂ bilayers (Fig. 1(a)) at the VBM around the K/K' states by resonant excitation at the K/K'-point. In this way IMBEs at the K/K' VBM can be probed by RILS spectroscopy at low temperatures providing experimental access to the moiré minibands caused by the geometrical superlattice in twisted bilayers as sketched in Fig. 1(b). Typical

* wurstbauer@uni-muenster.de

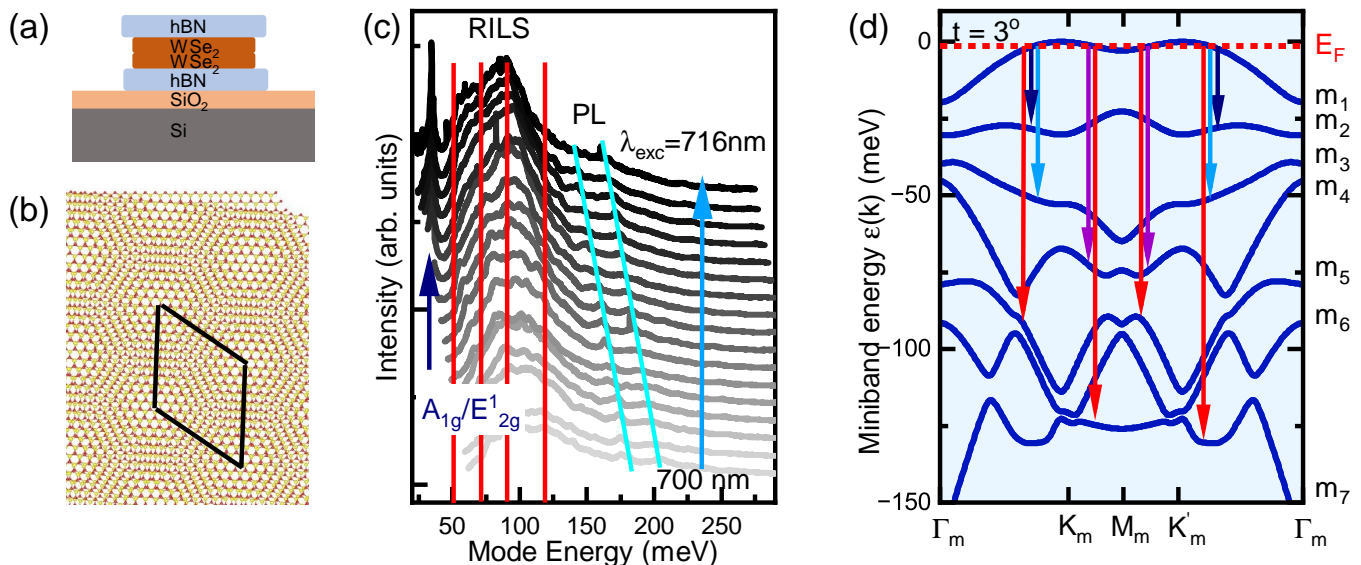


FIG. 1. (a) Scheme of the hBN encapsulated tWSe₂ bilayer. (b) Stick-ball model of a moiré-superlattice from a tWSe₂ bilayer with the moiré unit cell indicated. (c) RILS spectra on a 3° tWSe₂ bilayer. Spectra are offset for clarity. The A_{1g}, E_{2g}¹ phonons are indicated by a black arrow. The broad RILS signal are collective electronic inter-moiré band excitations (IMBE). The vertical red solid lines mark resonance energies from theoretically predicted transition energies. The tilted cyan line indicate emission signatures. [T = 4K, P_{Laser} = 1 mW]. (d) Calculated energy dispersion of the 7 highest moiré mini bands around the K, K' states for a 3° tWSe₂ bilayer. The minibands are labelled m₁, m₂, ...m₇. Exemplary inter-miniband transitions are sketched.

RILS spectra taken on a $\Theta \approx 3^\circ$ twisted WSe₂ bilayer at $T = 4\text{K}$ are shown in a water fall representation in Fig. 1(c). A rich spectrum of rather wide and dispersive RILS modes in addition to the sharp nearly degenerate optical active A_{1g}, E_{2g}¹ phonon modes appears at an energy range between $\approx 20\text{meV}$ and 120meV . Those excitation bands are in very good quantitative agreement with suitable IMB transitions extracted from the calculated electronic bands in the mini-BZ (mBZ) in the vicinity of the K/K' points. We obtain the band structures of tWSe₂ from a continuum model [1–4] with parameters adjusted to *ab-initio* simulations (for details see SI [32]). Fig. 1(d) summarizes the first seven moiré minibands with examples of vertical IMB transitions starting from the Fermi surface in the highest moiré band m₁.

We find that at the highest VBM minibands are rather flat with low energy separation of a few tens of meV for a twist angle around 3°, while the bands become nearly parabolic with a separation of several tens of meV for a twist angle of about 8° as will be discussed in more details below. Combined theoretical and experimental efforts, probing the moiré-bands via collective single-particle-like IMBE by RILS spectroscopy analogue to intersubband excitations in 2D charge carrier systems hosted e.g. in GaAs quantum wells [33–35] provides a promising approach to study the band structure of twisted transition metal dichalcogenides at twist angles where correlation physics play an important role [1, 12, 13, 16–18].

The hBN encapsulated tWSe₂ bilayers in this study

have been prepared by micromechanical cleavage using adhesive tape and viscoelastic dry transfer on top of Si/SiO₂ substrates using micro-manipulators with an estimated twist uncertainty of about $\pm 0.5^\circ$. To check for sufficient interlayer coupling and twist angle we employ non-resonant Raman spectroscopy (see SI [32]). An optical micrograph of a 3° tWSe₂ bilayer is displayed in inset of Fig. 2. Three different types of WSe₂ samples have been prepared with a twist of 3°, 8° and a natural homobilayer and characterized by low-temperature non-resonant Raman and photoluminescence (PL) measurements. For all measurements, the sample are mounted on the cold-finger of a closed-cycle refrigerator at a temperature of $T = 4\text{K}$. Position control is provided by x-y-z piezo actuators. The light from either a green solid state laser (2.33 eV) or a continuously tunable Ti:sapphire laser (linewidth of about 50 kHz) is focused with a cryogenic large-NA (NA = 0.82) objective lens to spot size of less than $2\mu\text{m}$. The emitted/scattered light is guided to the entrance slit of a triple grating spectrometer.

A typical PL spectrum for 3° tWSe₂ is displayed in Fig. 2. The emission is dominated by a broad asymmetric emission band peaking at around 1.65eV assigned to momentum and/or spin forbidden transitions from dark excitons that can only couple to light by interaction with suitable phonons [36]. In addition, charged excitons (trions), defect bound as well as charge-transfer excitons are supposed to contribute on the low-energy side of the emission band [36, 37]. A less intense emission line occurs

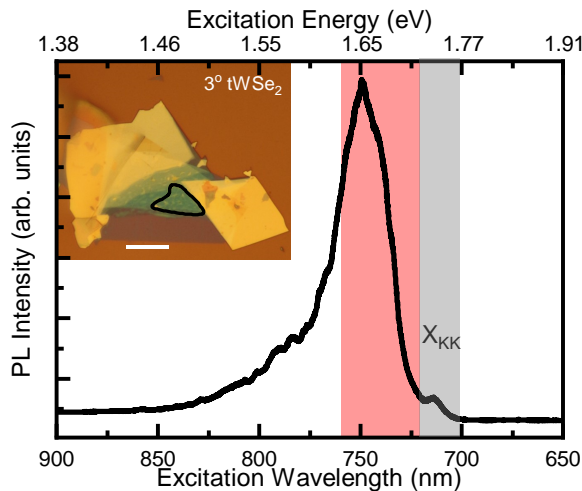


FIG. 2. (a) PL spectrum shows weak emission from direct K/K' excitons (X_{KK}) and a intense broad emission band from dark, charged and defect bound excitons. The spectral range around (X_{KK}) utilized for RILS spectroscopy is grey shaded and the region where modes in RILS are expected red shaded [$T = 4K$, $P_{\text{Laser}} = 1mW$, $E_{\text{Laser}} = 2.33eV$]. Inset: Optical micrograph of a hBN encapsulated 3° tWSe₂ sample with active region marked marked by black line. [scale bar $20\mu m$]

at higher-energy $\sim 1.74eV$ (grey-shaded spectral range). It originates from radiative recombination of Coulomb-coupled electron hole pairs residing at the same K or K' valley and hence includes a real VB state at the K/K' -points. This is important for resonant inelastic light scattering on collective charge excitations of a 2D hole system residing at the K/K' points of the moiré VBM [33, 35]. In RILS experiments the incident photon energies E_{Laser} is closely tuned to the energy of the X_{KK} -exciton observed in PL. The sample is excited by linearly polarized light in back-scattering geometry. Due to the large NA of the objective lens a bundle of in-plane momenta $q_{\parallel} < 2\omega_L/c\sin\theta_{\text{max}}$ with $\theta_{\text{max}} \approx 55^\circ$ is transferred to the hole system. Following the band-structure calculations shown in Fig. 1(d), the IMBE are expected in an energy range between $\sim 20meV$ and $\sim 120meV$. The resonance condition is given by the energy of the X_{KK} emission line. Following the consideration above, the energy range where we expect the IMBE in RILS is superimposed by the dark emission band marked by a red box in Fig. 2.

In Fig. 3, we contrast RILS spectra in a false color representation taken on 3° tWSe₂ (a), natural bilayer (NBL) WSe₂ (b) and 8° tWSe₂ (c). RILS intensities are plotted vs the relative energy (laser energy is at zero) with the intensity encoded in the color scheme. The well known Raman active phonon modes occur at the same energies as for the non-resonant measurements, however the intensities follow the expected resonance enhancement. In the RILS spectra of the twisted bilayers 3° tWSe₂ and 8° tWSe₂ displayed in Figs. 3(a) and (c), highly resonance,

intense and rather broad RILS modes interpreted as as IMBE dominate the RILS spectra. In addition to the phonon and IMBE resonances, a few features occur with energies depending on the incoming laser energy (tiled cyan lines) that are interpreted as defect or 0D-moiré potential localized emission signatures.

For the NBL sample despite the sharp phonon resonance, no clear RILS modes occur. The spectra are dominated by typical emission signatures. These lines are likely due to emission from interlayer excitons as expected for NBL layer [19]. The absence of RILS modes for NBL is expected due to the absence of moiré lattice and minibands. The energy separation of the SOI-split valence band is in the order of a few hundreds of meV [38] and hence far beyond the investigated energy range. For the 8° tWSe₂, instead, one weaker and one dominant broad RILS resonance appear at an energy range of about $60meV$ to $120meV$. For a quantitative comparison with theory, the related band structure for the moiré mBZ around the VBM at the K -point is displayed in Fig. 3 (d) in the experimentally relevant energy range (for extended range see SI ??). For such a large twist, the bands are nearly parabolic with larger energy separation. In comparison with theory, the weaker RILS mode at $\approx 60meV$ could be interpreted as a collective intra-band transition within the m_1 -band from the Fermi-edge to the local VBM. The more intense, broader RILS mode at $\approx 75 - 115 meV$ is interpreted as an IMBE $m_1 \rightarrow m_2$ transition with the broadening due to non-vertical transitions provided by the finite transferred in-plane momentum $q_{\parallel} \leq q_{\text{max}}$. The good quantitative agreement justifies our interpretation of the modes as being collective intra- and interband excitations allowing to study the band-structure of the mBZ at the K -points. To consider realistic twist-angle variations to be in the order of $\pm 0.3^\circ$. While the impact of twist angle variations is shown from calculated bands to be negligible small for $(8 \pm 0.3)^\circ$ tWSe₂, the impact is significant in the mini-band energy and dispersion for $(3 \pm 0.3)^\circ$ tWSe₂ as plotted in Fig. 3(e). Also here non-vertical transitions are expected due to finite momentum transfer q_{\parallel} in addition to defect induced breakdown of momentum conservation [39]. Twist angle variation together with non-vertical transitions are supposed to broaden IMBE signatures in RILS. The RILS modes are a convolution of jDOS and the momentum distribution, and a combined effect is most likely the reason that we do not observe well separated IMBE for the 3° tWSe₂. The extracted joint density of states (jDOS) in dependence of the position of E_F for a twist angle of 3° for the individual IMB transitions is plotted in Fig. 3(f). The jDOS demonstrate E_F -dependent IMB transitions $m_1 \rightarrow m_2$, $m_1 \rightarrow m_3$ and so on. Comparison between RILS spectra and the jDOS for $3 \pm 0.3^\circ$ tWSe₂ (Fig. 3(a,f)) provides a very good quantitative agreement with only the $m_1 \rightarrow m_2$ transition ($\approx 20 - 25meV$) being clearly separated. Also the

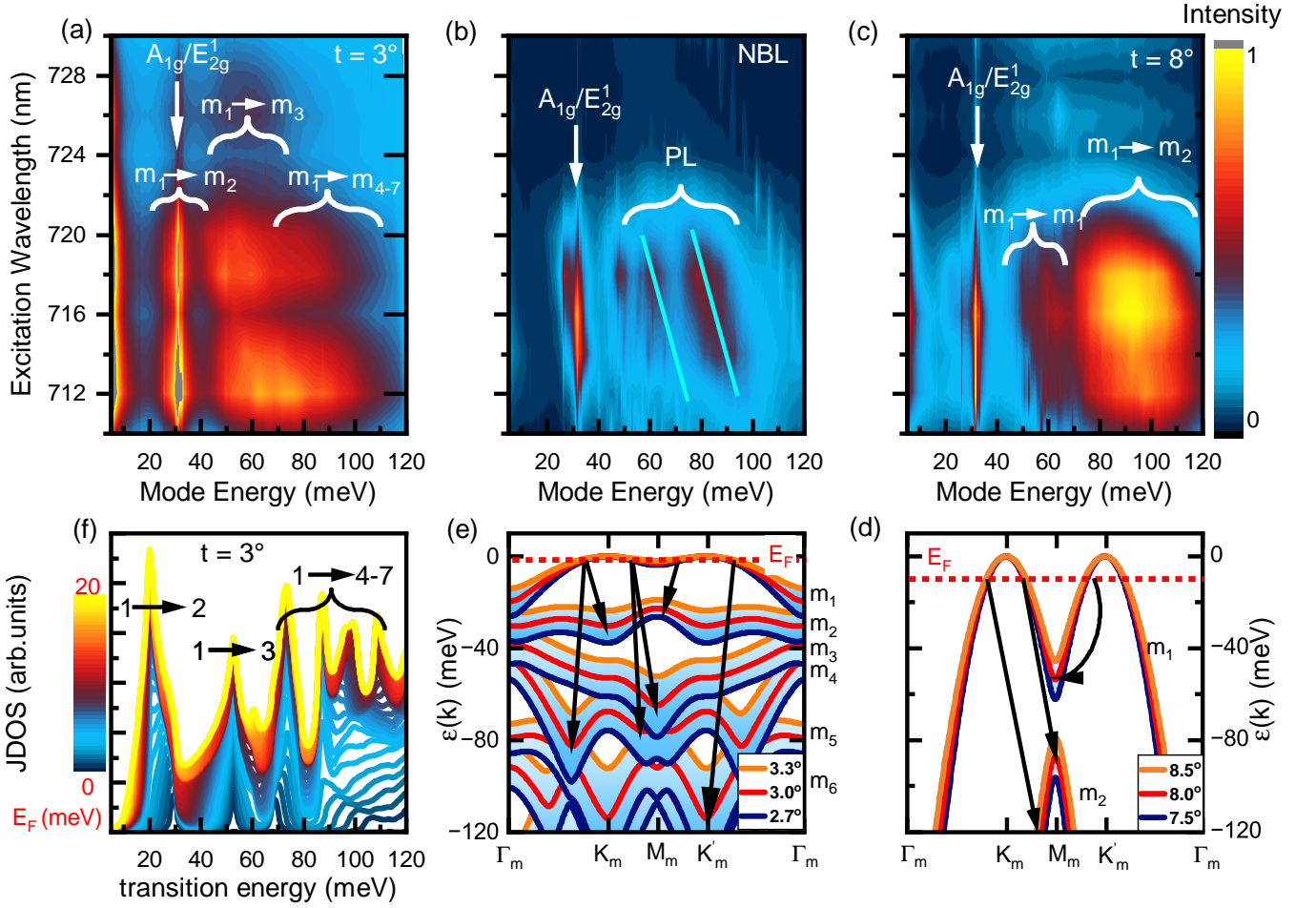


FIG. 3. RILS spectra on (a) 3° tWSe₂, (b) natural bilayer (NBL) and (c) WSe₂ 8° tWSe₂. The straight white arrows indicate phonon modes and the white curly braces in (a) and (c) IMBE with moiré band assignment according to calculations. In the natural bilayer spectra (b) in addition to the vertical phonon line only shifting emission signals marked with tilted cyan lines emerge. [$T = 4\text{K}$, $P_{\text{laser}} = 500\mu\text{W}$]. (d) Calculated electronic band structure for $(8^\circ \pm 0.5)^\circ$ considering realistic twist variations. (e) Calculated electronic band structure for $(3^\circ \pm 0.3)^\circ$. Twist variations can result in broadened mini-bands causing significantly broadened IMBE in RILS experiments. Breakdown of wave-conservation together with finite transferred in-plane momentum q_{\parallel} allows also for non-vertical transitions as indicated by the arrows. (f) Calculated joint density of states jDOS for IMB transitions in dependence of the Fermi-level E_F for 3° tWSe₂ for vertical transitions. E_F is given by the color code.

$m_1 \rightarrow m_3$ transition ($\approx 50 - 67\text{meV}$) can be identified and the $m_1 \rightarrow m_{4,5,6,7}$ transitions ($\approx 70 - 110\text{meV}$) are overlapping due to the discussed reasons of twist angle variations and finite momentum transfer q_{\parallel} . The experimental mode energies are in very good quantitative agreement with the transition from the jDOS. While the $m_1 \rightarrow m_2$ and $m_1 \rightarrow m_4$ transitions are nearly independent of E_F , position and particularly the intensity of the $m_1 \rightarrow m_2$ as well as $m_1 \rightarrow m_{5,6,7}$ are strongly dependent on E_F .

For this reason, excitation-power dependent RILS measurements for the 3° tWSe₂ sample are done in order to vary E_F by the photo-induced holes from $\Delta p \approx 10^9\text{cm}^{-2}$ to $\Delta p \approx 10^{10}\text{cm}^{-2}$ and $\Delta p \approx 10^{12}\text{cm}^{-2}$. Due to the strong band non-parabolicity and the unknown intrinsic doping it was not possible to estimate

the change in E_F from δp . In agreement with expectation from jDOS, the RILS intensity of mode assigned to IMBE $m_1 \rightarrow m_2$ is significantly reduced for the low density measurements (data shown in SI [32]). This comparison strongly supports our interpretation that the observed broad RILS signatures are indeed collective IMBE between moiré bands at the VBM.

To conclude, we establish that low-temperature RILS experiments on collective "single particle like" [33, 35, 40] IMBE on twisted WSe₂ bilayers is a powerful method to experimentally study the moiré band formation selectively at the VBM around the K/K' states, their energetic separation and twist angle dependence. We find several IMBE for a 3° tWSe₂ in an energy range between 20meV and 110 meV, while for a 8° tWSe₂ only one clear IMBE and presumably one collective intraband

excitation emerge in a similar energy range. RILS modes are absent for natural bilayers. These observations are in very good quantitative agreement with calculated band structures. In comparison with theory, we identify that twist angle variations significantly alters the energy dispersion for smaller twist angle. The observation of collective IMBE by RILS in a semiconducting vdW heterostructure demonstrates the potential to access the collective low-lying excitation spectra as unique fingerprints of individual quantum phases by RILS similar to correlated phases e.g. in the fractional quantum Hall effect regime [41, 42]. We would like to emphasize that collective excitation probe the weakly disordered parts of the sample, while disorder often results in the most dominant signatures in emission experiments and disturb transport investigations.

The authors gratefully acknowledge the German Science Foundation (DFG) for financial support via Grants WU 637/7-1, WE 5342/5-1 and the Priority Program SPP 2244 “2DMP” - 443273985, 443274199 as well as the computing time granted through JARA on the supercomputer JURECA [43] at Forschungszentrum Jülich. LK acknowledges support from the DFG through FOR 5249 (QUAST, Project No. 449872909). TW acknowledges support by the Cluster of Excellence ‘CUI: Advanced Imaging of Matter’ of the DFG (EXC 2056, Project ID 390715994). DMK acknowledges support by the Deutsche Forschungsgemeinschaft (DFG, German Research Foundation) under Germany’s Excellence Strategy - Cluster of Excellence Matter and Light for Quantum Computing (ML4Q) EXC 2004/1 - 390534769. We acknowledge support by the Max Planck-New York City Center for Nonequilibrium Quantum Phenomena.

-
- [1] D. M. Kennes, M. Claassen, L. Xian, A. Georges, A. J. Millis, J. Hone, C. R. Dean, D. N. Basov, A. N. Pasupathy, and A. Rubio, Moiré heterostructures as a condensed-matter quantum simulator, *Nature Physics* **17**, 155 (2021).
- [2] Y. Tang, L. Li, T. Li, Y. Xu, S. Liu, K. Barmak, K. Watanabe, T. Taniguchi, A. H. MacDonald, J. Shan, and K. F. Mak, Simulation of hubbard model physics in wse2/ws2 moiré superlattices, *Nature* **579**, 353 (2020).
- [3] F. Wu, T. Lovorn, E. Tutuc, and A. H. MacDonald, Hubbard Model Physics in Transition Metal Dichalcogenide Moiré Bands, *Physical Review Letters* **121**, 026402 (2018).
- [4] L. Balents, C. R. Dean, D. K. Efetov, and A. F. Young, Superconductivity and strong correlations in moiré flat bands, *Nature Physics*, 1 (2020).
- [5] P. A. Pantaleón, A. Jimeno-Pozo, H. Sainz-Cruz, V. T. Phong, T. Cea, and F. Guinea, Superconductivity and correlated phases in non-twisted bilayer and trilayer graphene, *Nat Rev Phys* **5**, 304 (2023).
- [6] Y. Cao, V. Fatemi, S. Fang, K. Watanabe, T. Taniguchi, E. Kaxiras, and P. Jarillo-Herrero, Unconventional superconductivity in magic-angle graphene superlattices, *Nature* **556**, 43 (2018).
- [7] Y. Cao, V. Fatemi, A. Demir, S. Fang, S. L. Tomarken, J. Y. Luo, J. D. Sanchez-Yamagishi, K. Watanabe, T. Taniguchi, E. Kaxiras, R. C. Ashoori, and P. Jarillo-Herrero, Correlated insulator behaviour at half-filling in magic-angle graphene superlattices, *Nature* **556**, 80 (2018).
- [8] Z. Hao, A. M. Zimmerman, P. Ledwith, E. Khalaf, D. H. Najafabadi, K. Watanabe, T. Taniguchi, A. Vishwanath, and P. Kim, Electric field-tunable superconductivity in alternating-twist magic-angle trilayer graphene, *Science* **371**, 1133 (2021).
- [9] J. M. Park, Y. Cao, K. Watanabe, T. Taniguchi, and P. Jarillo-Herrero, Tunable strongly coupled superconductivity in magic-angle twisted trilayer graphene, *Nature* **590**, 249 (2021).
- [10] Y. Zhang, R. Polski, C. Lewandowski, A. Thomson, Y. Peng, Y. Choi, H. Kim, K. Watanabe, T. Taniguchi, J. Alicea, F. von Oppen, G. Refael, and S. Nadj-Perge, Promotion of superconductivity in magic-angle graphene multilayers, *Science* **377**, 1538 (2022).
- [11] F. Wu, T. Lovorn, E. Tutuc, I. Martin, and A. H. MacDonald, Topological insulators in twisted transition metal dichalcogenide homobilayers, *Phys. Rev. Lett.* **122**, 086402 (2019).
- [12] J. Zang, J. Wang, J. Cano, and A. J. Millis, Hartree-fock study of the moiré hubbard model for twisted bilayer transition metal dichalcogenides, *Phys. Rev. B* **104**, 075150 (2021).
- [13] L. Xian, M. Claassen, D. Kiese, M. M. Scherer, S. Trebst, D. M. Kennes, and A. Rubio, Realization of nearly dispersionless bands with strong orbital anisotropy from destructive interference in twisted bilayer mos2, *Nature Communications* **12**, 5644 (2021).
- [14] L. Wang, E.-M. Shih, A. Ghiotto, L. Xian, D. A. Rhodes, C. Tan, M. Claassen, D. M. Kennes, Y. Bai, B. Kim, K. Watanabe, T. Taniguchi, X. Zhu, J. Hone, A. Rubio, A. N. Pasupathy, and C. R. Dean, Correlated electronic phases in twisted bilayer transition metal dichalcogenides, *Nature Materials* **19**, 861 (2020).
- [15] A. Ghiotto, E.-M. Shih, G. S. S. G. Pereira, D. A. Rhodes, B. Kim, J. Zang, A. J. Millis, K. Watanabe, T. Taniguchi, J. C. Hone, L. Wang, C. R. Dean, and A. N. Pasupathy, Quantum criticality in twisted transition metal dichalcogenides, *Nature* **597**, 345 (2021).
- [16] S. Ryee and T. O. Wehling, Switching between mott-hubbard and hund physics in moiré quantum simulators, *Nano Letters* **23**, 573 (2023).
- [17] L. Klebl, A. Fischer, L. Classen, M. M. Scherer, and D. M. Kennes, Competition of density waves and superconductivity in twisted tungsten diselenide, *Phys. Rev. Res.* **5**, L012034 (2023).
- [18] Y.-M. Wu, Z. Wu, and H. Yao, Pair-Density-Wave and Chiral Superconductivity in Twisted Bilayer Transition Metal Dichalcogenides, *Phys. Rev. Lett.* **130**, 126001 (2023).
- [19] Z. Wang, Y.-H. Chiu, K. Honz, K. F. Mak, and J. Shan, Electrical tuning of interlayer exciton gases in wse2 bilayers, *Nano Letters* **18**, 137 (2018), pMID: 29240440.
- [20] D. Halbertal, N. R. Finney, S. S. Sunku, A. Kerelsky, C. Rubio-Verdú, S. Shabani, L. Xian, S. Carr, S. Chen, C. Zhang, L. Wang, D. Gonzalez-Acevedo, A. S. McLeod, D. Rhodes, K. Watanabe, T. Taniguchi, E. Kaxiras, C. R.

- Dean, J. C. Hone, A. N. Pasupathy, D. M. Kennes, A. Rubio, and D. N. Basov, Moiré metrology of energy landscapes in van der waals heterostructures, *Nature Communications* **12**, 242 (2021).
- [21] T. I. Andersen, G. Scuri, A. Sushko, K. De Greve, J. Sung, Y. Zhou, D. S. Wild, R. J. Gelly, H. Heo, D. Bérubé, A. Y. Joe, L. A. Jauregui, K. Watanabe, T. Taniguchi, P. Kim, H. Park, and M. D. Lukin, Excitons in a reconstructed moiré potential in twisted WSe₂/WSe₂ homobilayers, *Nature Materials* **20**, 480 (2021).
- [22] E. Li, J.-X. Hu, X. Feng, Z. Zhou, L. An, K. T. Law, N. Wang, and N. Lin, Lattice reconstruction induced multiple ultra-flat bands in twisted bilayer WSe₂, *Nature Communications* **12**, 5601 (2021).
- [23] S. Zhao, Z. Li, X. Huang, A. Rupp, J. Göser, I. A. Vovk, S. Y. Kruchinin, K. Watanabe, T. Taniguchi, I. Bilgin, A. S. Baimuratov, and A. Högele, Excitons in mesoscopically reconstructed moiré heterostructures, *Nature Nanotechnology* 10.1038/s41565-023-01356-9 (2023).
- [24] M. Troue, J. Figueiredo, L. Sigl, C. Paspalides, M. Katzer, T. Taniguchi, K. Watanabe, M. Selig, A. Knorr, U. Wurstbauer, and A. W. Holleitner, Extended spatial coherence of interlayer excitons in mose₂/wse₂ heterobilayers, *Phys. Rev. Lett.* **131**, 036902 (2023).
- [25] O. Karni, E. Barré, V. Pareek, J. D. Georganas, M. K. L. Man, C. Sahoo, D. R. Bacon, X. Zhu, H. B. Ribeiro, A. L. O’Beirne, J. Hu, A. Al-Mahboob, M. M. M. Abdelrasoul, N. S. Chan, A. Karmakar, A. J. Winchester, B. Kim, K. Watanabe, T. Taniguchi, K. Barmak, J. Madéo, F. H. da Jornada, T. F. Heinz, and K. M. Dani, Structure of the moiré exciton captured by imaging its electron and hole, *Nature* **603**, 247 (2022).
- [26] A. Sood, J. B. Haber, J. Carlström, E. A. Peterson, E. Barre, J. D. Georganas, A. H. M. Reid, X. Shen, M. E. Zajac, E. C. Regan, J. Yang, T. Taniguchi, K. Watanabe, F. Wang, X. Wang, J. B. Neaton, T. F. Heinz, A. M. Lindenberg, F. H. da Jornada, and A. Raja, Bidirectional phonon emission in two-dimensional heterostructures triggered by ultrafast charge transfer, *Nature Nanotechnology* **18**, 29 (2023).
- [27] Z. Zhang, Y. Wang, K. Watanabe, T. Taniguchi, K. Ueno, E. Tutuc, and B. J. LeRoy, Flat bands in twisted bilayer transition metal dichalcogenides, *Nature Physics* **16**, 1093 (2020).
- [28] G. Gatti, J. Issing, L. Rademaker, F. Margot, T. A. de Jong, S. J. van der Molen, J. Teyssier, T. K. Kim, M. D. Watson, C. Cacho, P. Dudin, J. Avila, K. C. Edwards, P. Paruch, N. Ubrig, I. Gutiérrez-Lezama, A. F. Morpurgo, A. Tamai, and F. Baumberger, Flat Γ moiré bands in twisted bilayer wse₂, *Phys. Rev. Lett.* **131**, 046401 (2023).
- [2] H. Pan, F. Wu, and S. Das Sarma, Band topology, Hubbard model, Heisenberg model, and Dzyaloshinskii-Moriya interaction in twisted bilayer $\{\mathrm{WSe}\}_2$, *Physical Review Research* **2**, 033087 (2020).
- [3] T. Devakul, V. Crépel, Y. Zhang, and L. Fu, Magic in twisted transition metal dichalcogenide bilayers, *Nature Communications* **12**, 6730 (2021).
- [4] S. Ryee and T. O. Wehling, Switching between Mott-Hubbard and Hund Physics in Moiré Quantum Simulators, *Nano Letters* **23**, 573 (2023).
- [32] Supplementary Information.
- [33] A. Pinczuk, L. Brillson, E. Burstein, and E. Anastassakis, Resonant light scattering by single-particle electronic excitations in $n - \text{GaAs}$, *Phys. Rev. Lett.* **27**, 317 (1971).
- [34] G. Abstreiter, T. Egeler, S. Beeck, A. Seilmeier, H. Hübner, G. Weimann, and W. Schlapp, Electronic excitations in narrow gaas/algaas quantum well structures, *Surface Science* **196**, 613 (1988).
- [35] S. Das Sarma and D.-W. Wang, Resonant raman scattering by elementary electronic excitations in semiconductor structures, *Phys. Rev. Lett.* **83**, 816 (1999).
- [36] J. Lindlau, M. Selig, A. Neumann, L. Colombier, J. Förste, V. Funk, M. Förg, J. Kim, G. Berghäuser, T. Taniguchi, *et al.*, The role of momentum-dark excitons in the elementary optical response of bilayer wse₂, *Nature communications* **9**, 2586 (2018).
- [37] Z. Wang, Y.-H. Chiu, K. Honz, K. F. Mak, and J. Shan, Electrical tuning of interlayer exciton gases in wse₂ bilayers, *Nano Letters* **18**, 137 (2018).
- [38] A. Kormányos, G. Burkard, M. Gmitra, J. Fabian, V. Zólyomi, N. D. Drummond, and V. Fal’ko, Corrigendum: k.p theory for two-dimensional transition metal dichalcogenide semiconductors (2015 2d mater. 2 022001), *2D Materials* **2**, 049501 (2015).
- [39] U. Wurstbauer, D. Majumder, S. S. Mandal, I. Dujovne, T. D. Rhone, B. S. Dennis, A. F. Rigosi, J. K. Jain, A. Pinczuk, K. W. West, and L. N. Pfeiffer, Observation of nonconventional spin waves in composite-fermion ferromagnets, *Phys. Rev. Lett.* **107**, 066804 (2011).
- [40] S. Meier, P. E. F. Junior, F. Haas, E.-S. Heller, F. Dirnberger, V. Zeller, T. Korn, J. Fabian, D. Bougeard, and C. Schüller, Intersubband excitations in ultrathin core-shell nanowires in the one-dimensional quantum limit probed by resonant inelastic light scattering, *Phys. Rev. B* **104**, 235307 (2021).
- [41] U. Wurstbauer, K. W. West, L. N. Pfeiffer, and A. Pinczuk, Resonant inelastic light scattering investigation of low-lying gapped excitations in the quantum fluid at $\nu=5/2$, *Phys. Rev. Lett.* **110**, 026801 (2013).
- [42] L. Du, U. Wurstbauer, K. W. West, L. N. Pfeiffer, S. Fallahi, G. C. Gardner, M. J. Manfra, and A. Pinczuk, Observation of new plasmons in the fractional quantum hall effect: Interplay of topological and nematic orders, *Science Advances* **5**, eaav3407 (2019).
- [43] Jülich Supercomputing Centre, JURECA: Data Centric and Booster Modules implementing the Modular Supercomputing Architecture at Jülich Supercomputing Centre, *Journal of large-scale research facilities* **7**, 10.17815/jlsrf-7-182 (2021).

Supplemental Materials: Collective charge excitations between moiré-minibands in twisted WSe₂ bilayers from resonant inelastic light scattering

METHODS AND EXPERIMENTAL PROCEDURE

Sample preparation

The tWSe₂ samples were prepared by first mechanically exfoliating the monolayer WSe₂ and multilayer hBN crystals onto viscoelastic PDMS stamps followed by their deterministic dry transfer (DDT) using a home-built setup with x-y-z and rotational micro-manipulators. To fix the stacking (twist) angle between the WSe₂ monolayers, their crystalline edges were determined from optical images on the PDMS stamps. Following this, the top WSe₂ monolayer was stacked on top of the bottom WSe₂ monolayer at the desired twist angle by using a rotation stage attached to the sample stage in the DDT setup. After preparation of the full heterostructure including the hBN encapsulation layers, the samples were annealed under a home-built vacuum annealing chamber at 100 - 120 °C for 5 - 6 hours.

Non-resonant photoluminescence (PL) and Raman spectroscopy

After preparation of the samples, they were characterized by low temperature non-resonant PL and Raman spectroscopies. The samples were mounted on the cold finger equipped with x-y-z piezo stages of a dilution refrigerator. The samples were cooled down to 4K using pulse tube refrigeration operating with helium gas. For non-resonant characterization measurements, a 532 nm (2.33 eV) solid state laser, cleaned up using a grating based monochromator with a 1nm bandpass, was used for excitation of the samples. The laser was focused on the samples with a low temperature compatible objective lens with an NA of 0.82 mounted on a homebuilt stage attached to the 4K stage of the refrigerator. The focused spot on the sample had a diameter of $\sim 2\mu\text{m}$. The emission and scattering signals from the sample were collected by the same objective lens in a back scattering geometry and dispersed using a single spectrometer with a 600 l/mm grating for PL and an 1800 l/mm grating for Raman spectroscopy. The focal length of the spectrometer was 750 mm and the spectral resolution (532 nm, 1800 l/mm grating) was $\sim 0.4\text{ cm}^{-1}$. The Rayleigh scattered light was filtered out by using a 532 nm long pass filter in front of the spectrometer. The dispersed light was collected and measured using a liquid nitrogen cooled CCD camera. Position and laser power dependent PL and position dependent Raman measurements were used to select the region of the sample for subsequent resonant inelastic light scattering measurements.

Resonant Inelastic Light Scattering spectroscopy

Following the characterization by low temperature PL and Raman spectroscopy, inelastic light scattering spectra under resonant excitation conditions were measured. The samples were mounted inside a dilution refrigerator as described above. The samples were excited at energies between 1.698 eV (730 nm) and 1.771 eV (700 nm) using a continuously frequency tunable Ti:sapphire laser stabilized by a ring cavity with a linewidth of about 50kHz. The luminescence background from the Ti:sapphire crystal was removed by passing the excitation laser beam through a monochromator (1nm bandpass). The light emitted or scattered from the sample surface were again collected in back scattering geometry and sent to either a single spectrometer with a 600 l/mm grating or to a triple spectrometer with a grating combination of 300 l/mm, 300 l/mm and 600 l/mm. The triple spectrometer was used in a subtractive mode where the second stage of the spectrometer is used to suppress the dispersion generated by the first stage by appropriate alignment of the gratings. This meant that at the exit slit of the second stage, light could be filtered out based on the angle of entrance in the spectrometer. Thus, the first two stages served as a bandpass filter and filtered out any stray light not following the path of light scattered from the sample, as well as the Rayleigh scattered background.

THEORETICAL CALCULATIONS

Continuum Hamiltonian

In the small-angle approximation $\Theta \sim 0^\circ$, the dispersion of tWSe₂ can be obtained by constructing a continuum model (following Refs. [S1–S4]). As the electrons in a WSe₂ monolayer are spin-valley locked, only one valley per layer contributes to each spin sector of the moiré Hamiltonian

$$H_\uparrow(\mathbf{k}) = \begin{pmatrix} -\frac{\hbar^2(\mathbf{k}-K_1)^2}{2m^*} + \Delta_1(\mathbf{r}) & \Delta_T(\mathbf{r}) \\ \Delta_T^\dagger(\mathbf{r}) & -\frac{\hbar^2(\mathbf{k}-K_2)^2}{2m^*} + \Delta_2(\mathbf{r}) \end{pmatrix} \quad (\text{S1})$$

where $m^* = 0.43 m_e$ is the effective mass, K_l the original K -point of layer $l = 1, 2$, $\Delta_T(\mathbf{r})$ the interlayer potential, and $\Delta_l(\mathbf{r})$ the intralayer potential. The other spin sector $H_\downarrow(\mathbf{k})$ is obtained from time reversal symmetry. The inter- and intralayer potentials are parameterized by the following simple formulæ:

$$\Delta_l(\mathbf{r}) = 2V \sum_{\mathbf{g} \in \Delta} \cos(\mathbf{g} \cdot \mathbf{r} + \sigma_z^l \psi), \quad \Delta_T(\mathbf{r}) = w \sum_{\mathbf{g} \in \Delta} e^{-i\mathbf{g} \cdot \mathbf{r}}. \quad (\text{S2})$$

Here, σ_z is the Pauli z matrix and \mathbf{g} are three reciprocal moiré lattice vectors that are connected by C_3 rotations. Hence we index the summation over those three reciprocal moiré lattice vectors as $\mathbf{g} \in \Delta$. The K - and K' -points in the moiré Brillouin zone (BZ) coincide with K_1 and K_2 , respectively.

The intralayer potential strength $V = 9$ meV, the interlayer hopping $w = 18$ meV, and the intralayer potential parameter $\psi = 128^\circ$ are taken to match density functional theory results [S3]. Note that the twist angle Θ enters Eq. (S1) through geometry in the momentum argument \mathbf{k} as well as the length of the inverse moiré lattice vectors \mathbf{g} in Eq. (S2).

For numerical diagonalization of the Hamiltonian Eq. (S1), the expansion in inverse moiré lattice vectors must be truncated. We take into account the following inverse moiré lattice vectors \mathbf{G}

$$\mathbf{G} \in \{\mathbf{H} \mid \|\mathbf{H}\| \leq 3\|\mathbf{g}\| \ \forall \ \mathbf{g} \in \Delta\}, \quad (\text{S3})$$

i.e., a distance shell cutoff with length 3, which is sufficient for convergence of the resulting band structures.

Joint Density of States

The joint density of states (jDOS) data in Fig. 3 (f) of the main text is obtained numerically from the model discussed above. In essence, we implement the following formula:

$$\text{jDOS}(\omega) = \text{Im} \sum_{\mathbf{k}, b_1, b_2} \frac{f(\epsilon_{b_1}(\mathbf{k})) - f(\epsilon_{b_2}(\mathbf{k}))}{\omega - i\eta + \epsilon_{b_1}(\mathbf{k}) - \epsilon_{b_2}(\mathbf{k})}, \quad (\text{S4})$$

where $\epsilon_b(\mathbf{k})$ is the dispersion of band b with \mathbf{k} in the mini BZ, $f(x) = (1 + \exp[\beta(x - \mu)])^{-1}$ the Fermi function, and $\eta = 5$ meV a Lorentzian broadening. The inverse temperature is set to $\beta = 10^2$ meV⁻¹. As we perform massive scans in frequency ω and chemical potential μ (Fermi energy) for significant \mathbf{k} -meshes (96×96 regularly spaced points in the primitive zone), we make use of the parallel nature of Eq. (S4) using a custom GPU implementation.

ADDITIONAL FIGURES

Non-resonant Raman measurements

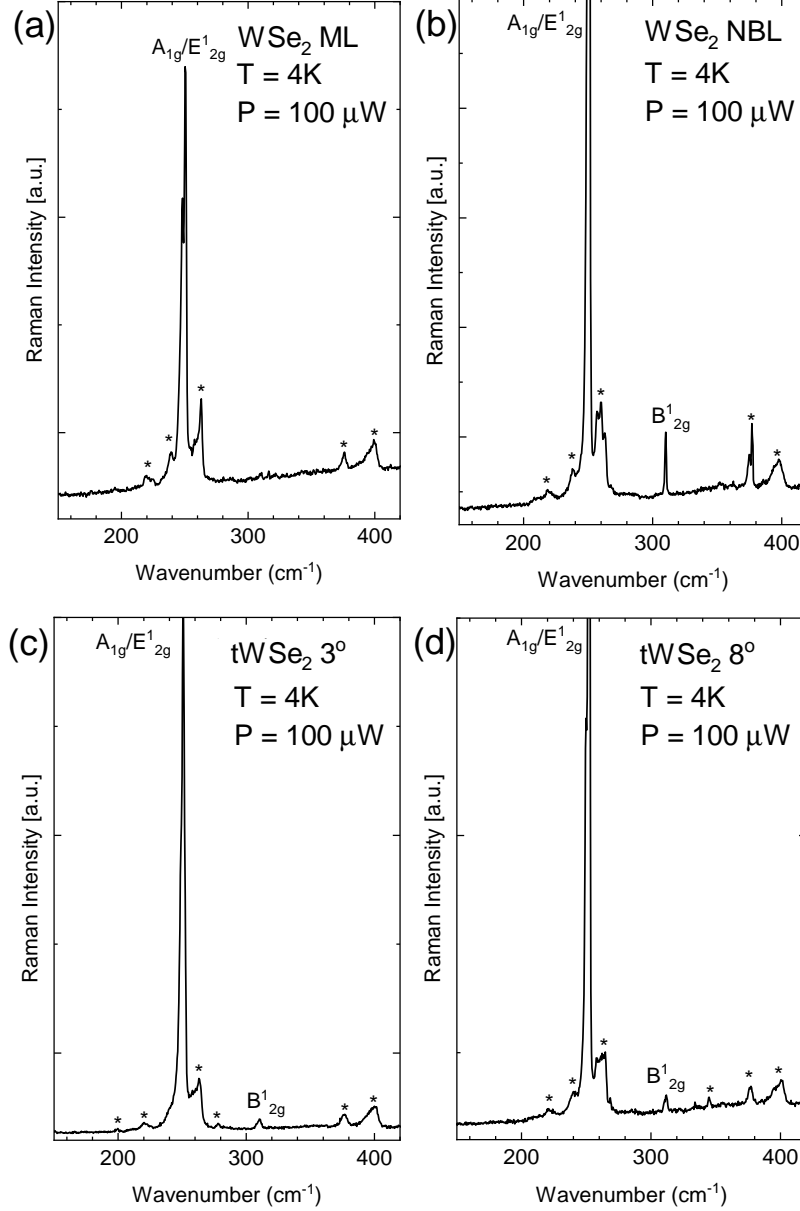


FIG. S1. (c) Non-resonant Raman spectra on hBN encapsulated WSe₂ monolayer (a), hBN encapsulated natural bilayer (NBL) WSe₂ (b), hBN encapsulated 3° tWSe₂ (c) and hBN encapsulated 8° tWSe₂. All spectra show the optical phonon modes A_{1g}, E_{2g}¹ and in addition the NBL and twisted bilayer show the B_{2g}¹ phonon mode. The features marked by an asterisk (*) are due to multiphonon scattering processes [T = 4K, P_{laser} = 100 μW, E_{laser} = 2.33 eV].

Excitation Power dependent RILS measurements

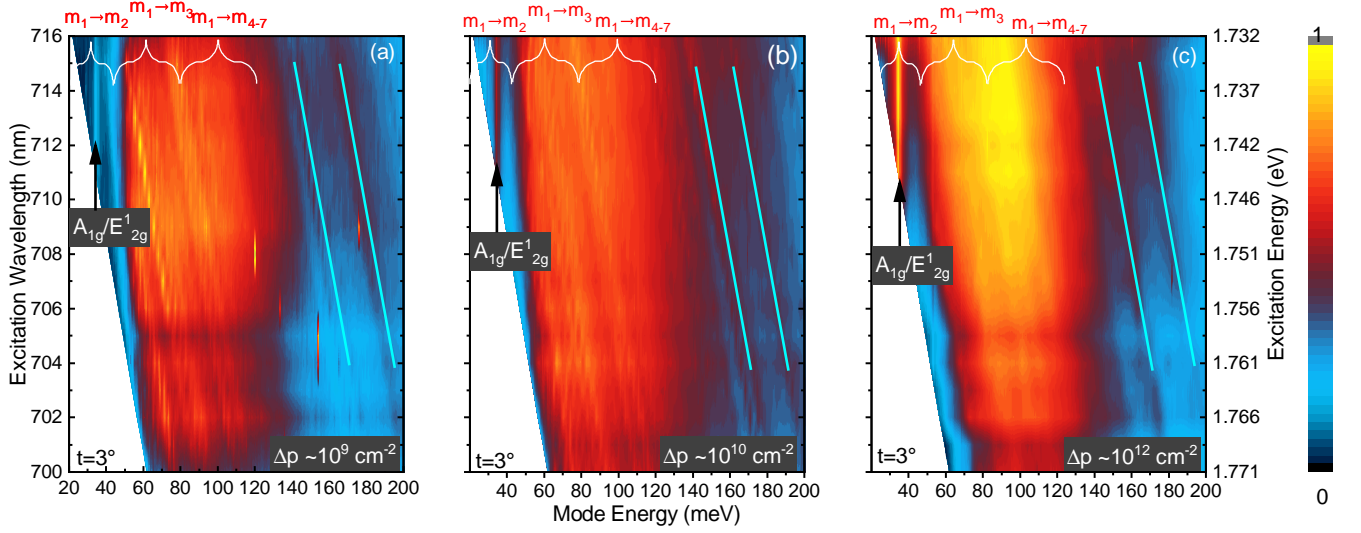


FIG. S2. (a) False color plots of RILS spectra for 3° tWSe₂ at three different excitation powers of (a) $1\mu\text{W}$, (b) $50\mu\text{W}$ and (c) 1mW , respectively. The corresponding photo-excited hole-densities are $\sim 10^9\text{ cm}^{-2}$, $\sim 10^{10}\text{ cm}^{-2}$ and $\sim 10^{12}\text{ cm}^{-2}$, respectively. The phonon-lines are marked by straight arrows and emission features by tilted cyan solid lines. White braces indicate the energy positions of IMBE. Particularly the $m_1 \rightarrow m_2$ transition is enhanced with increasing doping and hence position of E_F in agreement with $\text{jDOS}(E_F)$ [$T = 4\text{K}$].

Excitation-power dependent RILS measurements are performed for the 3° tWSe₂ sample in order to vary E_F by the photo-induced holes. RILS spectra from a different set of experiments are compared in Fig. S2 for (a) $1\mu\text{W}$ corresponding to a change in the hole density by $\delta p \approx 10^9\text{ cm}^{-2}$, (b) $50\mu\text{W}$ ($\delta p \approx 10^{10}\text{ cm}^{-2}$) and (c) 1mW ($\delta p \approx 10^{12}\text{ cm}^{-2}$), respectively. Due to the strong band non-parabolicity and the unknown intrinsic doping it is not possible to estimate the change in E_F from δp . While it is not possible within the experimental certainty to clearly identify a shift in the energy, the intensity of the RILS mode assigned to IMBE $m_1 \rightarrow m_2$ is significantly reduced for the low density measurements as expected from the jDOS . Similarly, for the high energy transition that seems to be most pronounced for the higher power measurements indicated by an even broader overlapping emission band towards 100meV and beyond. This is most pronounced for $50\mu\text{W}$. For the 1mW spectra some spectral weight shifts back to the intermediate transitions regions $m_1 \rightarrow m_{4,5}$. This also agrees with the jDOS from the band structure calculation and strongly supports our interpretation that the observed broad RILS signatures are indeed collective IMBE between moiré bands at the VBM.

Calculated mini-band structure

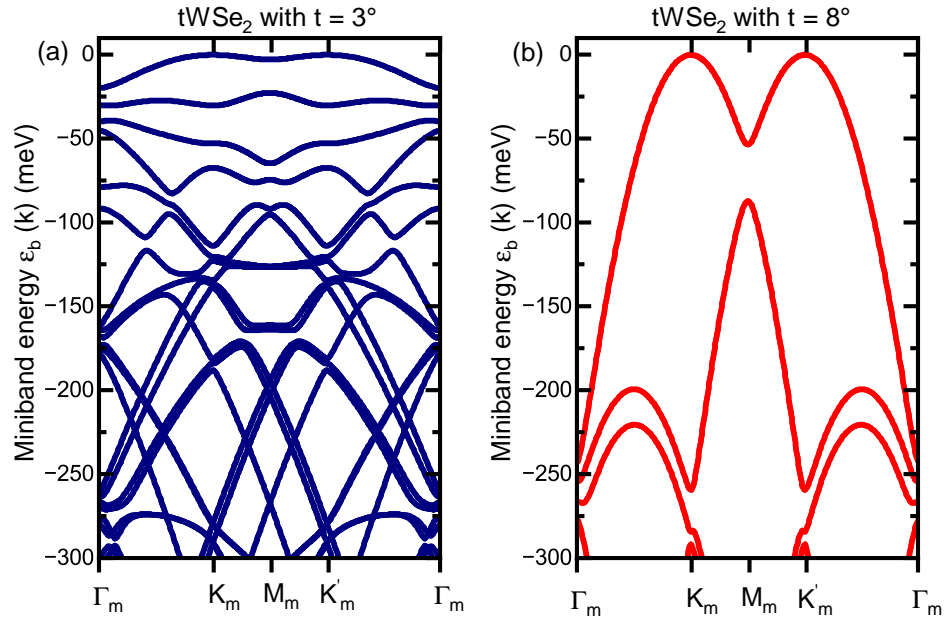


FIG. S3. Calculated energy dispersion of the highest moiré mini bands down to -300meV around the K, K' states for a 3° tWSe₂ bilayer (a) and a 8° tWSe₂ bilayer (b).

-
- [S1] F. Wu, T. Lovorn, E. Tutuc, and A. H. MacDonald, Hubbard Model Physics in Transition Metal Dichalcogenide Moiré Bands, *Physical Review Letters* **121**, 026402 (2018).
- [S2] H. Pan, F. Wu, and S. Das Sarma, Band topology, Hubbard model, Heisenberg model, and Dzyaloshinskii-Moriya interaction in twisted bilayer WSe_2 , *Physical Review Research* **2**, 033087 (2020).
- [S3] T. Devakul, V. Crépel, Y. Zhang, and L. Fu, Magic in twisted transition metal dichalcogenide bilayers, *Nature Communications* **12**, 6730 (2021).
- [S4] S. Rye and T. O. Wehling, Switching between Mott-Hubbard and Hund Physics in Moiré Quantum Simulators, *Nano Letters* **23**, 573 (2023).